Academic Journal of Science and Technology
ISSN: 2771-3032 | Vol. 23, No. 2, 2026

Damage Evolution and Infrared Precursory Characteristics of Sandstone Containing Stress-Relief Holes

Shihan Sun[1], Shangshu Sun[1], Tiebin Chen[1], Jiayi Ma[1], Yuan Chang[1,*]

[1]School of Civil Engineering, University of Science and Technology Liaoning, Anshan, Liaoning 114051, China

[*] Corresponding author

Abstract: To investigate how the diameter of stress-relief holes affects the load-bearing capacity and damage evolution of sandstone, intact Qing sandstone specimens and specimens containing holes with diameters of 6, 8, 10, and 12 mm were comparatively evaluated. The relationships between hole diameter and mechanical response were examined using uniaxial compression stress-strain curves, failure photographs, acoustic-emission (AE) ring counts, and energy-evolution curves. The peak strength of the intact specimens was 30.95 MPa, and the peak strengths of the four holed groups were 18.73, 18.68, 17.34 and 15.32 MPa, respectively. The elastic modulus of the undamaged specimen was 4.80 GPa; that of the specimen with a 12-mm hole was 1.60 GPa. The maximum strain of the holed specimen exceeded that of the undamaged specimen, and therefore, a reduction in load-bearing capacity was accompanied by an increase in pre-peak deformation. Failure photographs showed that regions adjacent to the holes participated in the formation of the main cracks; longitudinal cracks, inclined cracks, and branching cracks developed in the holed specimens. AE activity generally intensified with loading, but neither the peak ring count nor the cumulative count varied monotonically with hole diameter. In the latter stages of loading, the energy curves showed decreasing releasable elastic strain energy and increasing dissipated energy. The possible relationship between hole-wall damage and infrared anomalies is discussed, and the dependence of infrared precursors on hole diameter is identified as requiring validation with synchronous temperature-field data. These results provide experimental reference for damage identification in holed sandstone and for evaluating load-bearing constraints in the design of pressure-relief holes.

Keywords: Sandstone; Stress-relief hole; hole diameter; Damage evolution; Acoustic emission; Infrared precursor.

1. Introduction

As coal-resource extraction extends to greater depths, the stability of surrounding rock and the prevention of dynamic disasters under high in situ stress have become increasingly important. Deep mining involves adjustments to the initial stress field, excavation unloading, and mining-induced disturbances, causing deformation and failure of rock masses to be governed by increasingly complex stress conditions. Ranjith et al. [1] identified high in situ stress, rockburst, and large deformation as major rock-mechanics challenges in deep mineral-resource extraction. From the perspective of static-dynamic load coupling, Li et al. [2] further discussed failure mechanisms in deep hard rock and emphasized that the initial stress state and external disturbances jointly contribute to instability. Accordingly, investigating damage development, energy conversion, and observable responses in loaded rock is essential for understanding failure mechanisms in deep surrounding rock and for developing disaster-monitoring methods.

Borehole pressure relief introduces a local free boundary into the surrounding rock, thereby modifying the stress distribution and load-transfer path and providing space for local deformation and stress release. Lu et al. [3] conducted pressure-relief tests on sandstone containing boreholes under high-stress conditions and analyzed stress variation and energy dissipation during drilling, showing that the drilling configuration affects the pressure-relief response. However, a hole also weakens structural continuity, and its effects on stress redistribution and load-bearing capacity must be evaluated together. Wu et al. [4] combined digital image correlation with AE monitoring to investigate fracture processes in holed sandstone and found that the hole and its shape affect mechanical properties, the stress distribution around the hole, and crack evolution. Li and other [5] performed uniaxial compression tests on rock-like materials with different hole diameters relative to specimen size, further demonstrating that the relative hole size is closely related to peak strength, elastic modulus, and failure mode. These studies provide a basis for understanding failure in holed rock masses; however, results obtained for different materials, hole geometries, and loading conditions cannot be directly substituted for one another. For natural sandstone, the effects of hole diameter on load bearing, deformation, and damage evolution should therefore be examined under otherwise comparable conditions.

Infrared thermography provides non-contact, continuous observation and imaging of surface temperature fields, offering spatial information for identifying damage in loaded rock. Ma et al. [6] conducted infrared-radiation tests on sandstone under uniaxial loading, providing experimental evidence for interpreting radiation responses during loading. Wu et al. [7] compared infrared-image anomalies associated with rock fracture under different loading conditions and discussed their morphology and thermomechanical mechanisms. From an energy-conversion perspective, Sun et al. [8] analyzed sandstone damage evolution and examined the relationship between elastic strain-energy release, dissipated-energy variation, and anomalies in infrared-radiation counts. Infrared response, however, does not necessarily manifest as a simple warming process. Sun et al. [9] noted that thermoelastic effects, friction on crack surfaces,

and changes in pore gas may jointly contribute to surface-temperature variation in sandstone, with their dominant roles changing across damage stages. On this basis, Sun et al. [10] explored the potential of infrared-radiation counts for identifying sandstone damage, providing a reference for extracting local radiation anomalies. Meanwhile, infrared signals are susceptible to ambient-temperature variation and instrument drift. The background thermal-noise correction method proposed by Sun et al. [11] indicates that separating load-related signals from background variation is necessary for interpreting infrared responses.

AE records transient elastic waves released by crack activity and provides time-series information for analyzing internal rock fracture. He et al. [12] analyzed AE spectra and energy variation during rockburst in limestone under true-triaxial unloading and showed that AE responses can reflect the development of fracture activity. By contrast, infrared thermography primarily characterizes the radiation state of the visible surface; the two techniques are therefore complementary in terms of their observation targets and spatial scales. Liu et al. [13] conducted synchronous AE and infrared-monitoring tests on sandstone and analyzed infrared-temperature variation at different stages of crack evolution, demonstrating that AE information can help interpret surface-radiation responses. Zhao and Jiang [14] compared AE and infrared precursors in bump-prone coal under different loading conditions, while Sun et al. [15] applied the two monitoring methods to the rockburst process in rock specimens. These studies show that joint analysis of multiple signals can improve understanding of failure processes; nevertheless, monitoring responses remain constrained by material properties, stress paths, and observation conditions. The anomalous timing and warning indicators reported in previous studies cannot be transferred directly to sandstone specimens with different hole diameters. The relationships among hole diameter, fracture activity, energy conversion, and infrared response therefore require verification using corresponding data.

Accordingly, intact Qing sandstone and specimens containing stress-relief holes with diameters of 6, 8, 10, and 12 mm were investigated. The stress-strain relationship, peak strength, elastic modulus, peak strain, and macroscopic failure morphology under uniaxial compression were compared. AE ring counts and energy-evolution curves were further used to analyze damage development in specimens with different hole diameters. The possible relationship between hole-wall damage and infrared-radiation anomalies is then discussed, providing reference for damage identification in holed sandstone and for evaluating load-bearing capacity in the design of pressure-relief holes.

2. Experimental Materials and Analytical Methods

2.1. Specimens and Hole-Diameter Groups

The test material was Qing sandstone. The specimens were machined to 50 mm × 50 mm × 100 mm. Intact specimens served as controls. The holed specimens were designated R3, R4, R5, and R6, corresponding to borehole radii of 3, 4, 5, and 6 mm, or hole diameters of 6, 8, 10, and 12 mm, respectively. Throughout this paper, the hole diameter d is used as the comparison variable to avoid confusion between radius and diameter. The ratios of hole diameter to specimen width were 0.12, 0.16, 0.20, and 0.24, respectively, representing the hole size relative to the specimen transverse dimension.

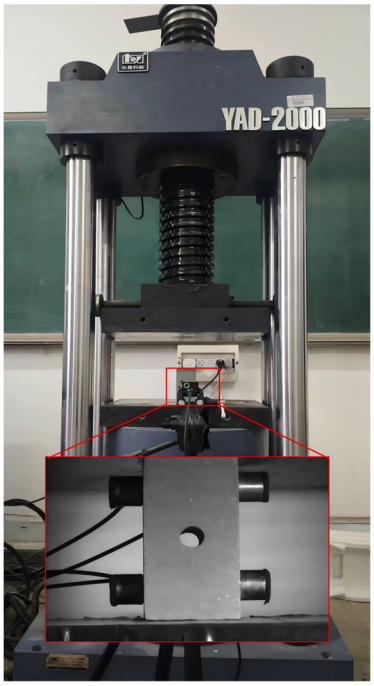
Table 1. Experimental parameter scheme

Borehole parameters	Specimen photographs				
Different borehole diameters R (through-hole)					
	Intact specimen I	R3	R4	R5	R6

2.2. Experimental Equipment

Uniaxial compression was performed using a hydraulic loading system under displacement control, together with an AE analyzer, an infrared thermal imager, and a camera (Figure 1). Before loading, specimen dimensions were marked, AE sensors were installed, and the imaging equipment was arranged. Stress-strain data and AE responses were recorded during loading, and crack morphology was examined after failure. The analysis used comparative plots of mechanical parameters, failure photographs, four AE-count plots, and energy-evolution plots

An AE ring count is the number of times a signal exceeds a preset threshold. A single fracture process may produce multiple threshold crossings; therefore, a ring count cannot be equated directly with the number of cracks. Comparisons between groups are also affected by sensor coupling, threshold selection, amplifier gain, and sampling procedures. Because complete waveforms and acquisition parameters were unavailable, this study focuses primarily on stage-wise changes within each curve and on differences that can be observed directly between hole-diameter groups.



(a) High-speed camera for the loading system



(b) Infrared monitoring system





(c) AE acquisition system

Figure 1. Experimental loading and monitoring system

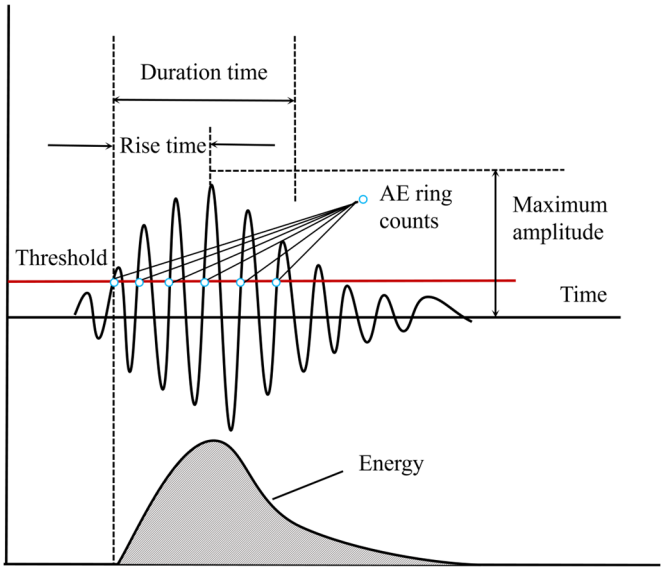


Figure 2. Schematic illustration of an AE waveform and its characteristic parameters

3. Mechanical Response of Sandstone with Different Hole Diameters

3.1. Stress-Strain Curves

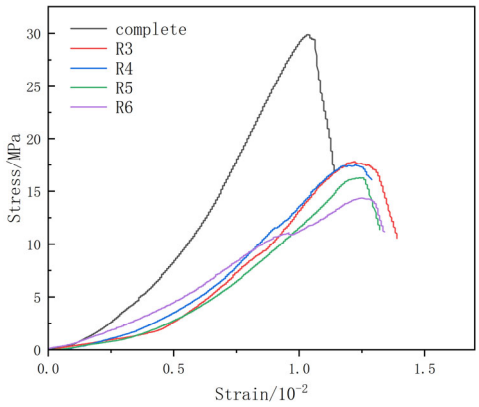
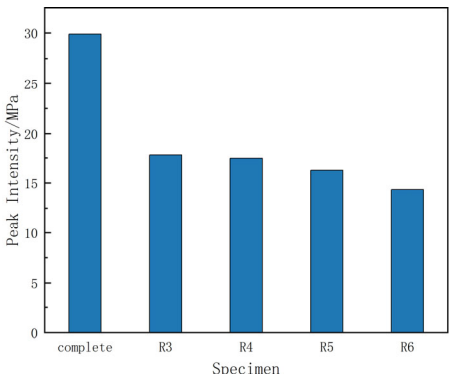


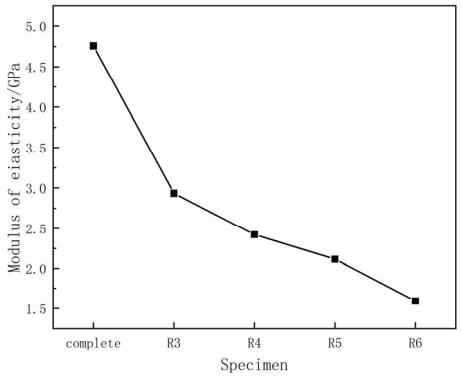
Figure 3. Stress-strain curves of specimens with different hole diameters

As shown in Figure 3, all the specimens had an initial concave-up stress-strain curve, followed by a region of rapid stress increase and a post-peak decline. The curve of the undamaged specimen is higher than that of the hollow specimen in the loading range, and the stress at the same axial strain is larger. An increase in the diameter of the hole generally causes a downward shift of the curve of the holed specimen and reduces both its load-bearing capacity and deformation capacity.The initial nonlinearity may result from the combined effects of closure of pre-existing pores, microcrack adjustment, and the contact condition between the specimen and platens. The individual contributions of the factors in this section cannot be identified, and the differences among the hole-diameter groups should not be solely attributed to drilling damage. In the high-stiffness regime, the reduction of curve slope with an increase in hole diameter is relatively pronounced; at this time, load bypass around the hole and deformation near the hole may significantly alter the overall response. The peak stress reduction of the undamaged specimen is relatively high, and the holed specimen also exhibits post-peak softening. The Lengths of the descending post-peak sections are not the same. Therefore, one should not draw conclusions about the gradualness of failure or the rank of brittleness of the holed specimens solely from the plotted curves based on hole diameter. The Criteria for brittleness and the entire post-peak response of loading-system stiffness and crack-evolution process must be specified.

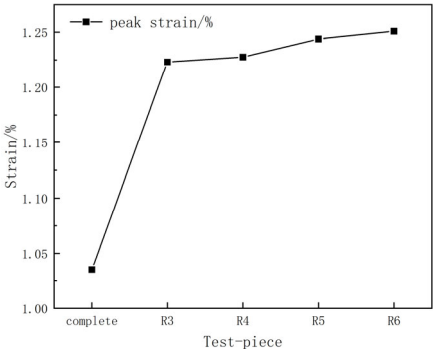
3.2. Mechanical Parameters



(a) Peak strength



(b) Elastic modulus



(c) Peak strain

Figure 4. Mechanical parameters of specimens with different hole diameters

The presence of a hole substantially weakens the load-bearing capacity of the specimens. The intact specimens had a peak strength of 30.95 MPa, whereas the holed specimens had strengths of 15.32-18.73 MPa over the 6-12 mm diameter range, corresponding to reductions of 39.48%-50.50%. When the diameter increased from 6 to 8 mm, peak strength decreased only slightly, from 18.73 to 18.68 MPa, and the strength reduction remained nearly unchanged. With further increases to 10 and 12 mm, peak strength decreased to 17.34 and 15.32 MPa, corresponding to reductions of 43.97% and 50.50%, respectively. Thus, the marginal weakening effect of a hole is relatively limited at small diameters, whereas the loss of load-bearing capacity becomes more pronounced at larger diameters.

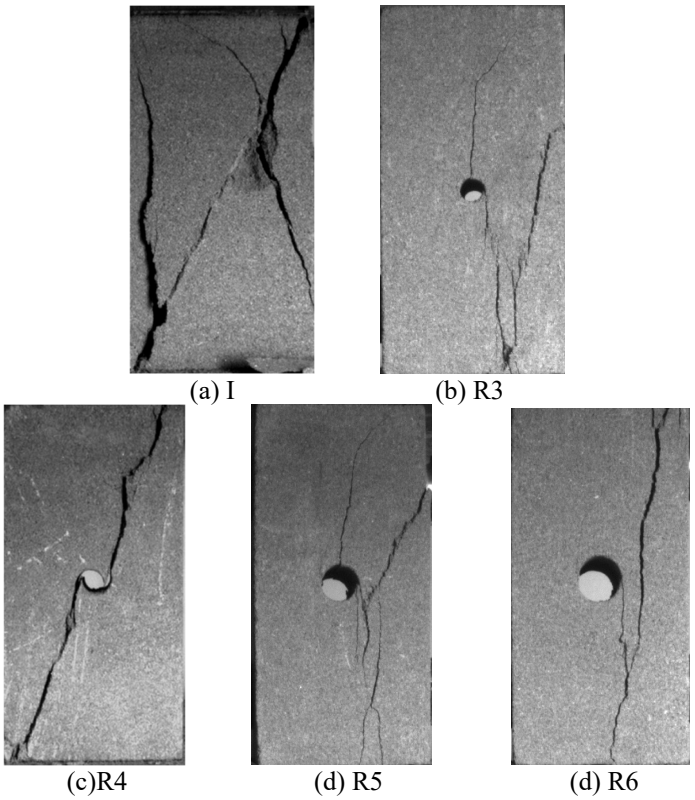
The evolution of elastic modulus further confirms the continuous degradation of specimen stiffness caused by the hole. The elastic modulus of the intact specimen was 4.80 GPa, and the moduli of the holed specimens decreased with increasing diameter to 2.95, 2.45, 2.10, and 1.60 GPa for R3-R6, respectively. The Modulus of R6 was approximately 66.7% lower than that of the undamaged sample. The modulus of elasticity is more sensitive to changes in hole size than the maximum stress, and there is no strength-like plateau at R3 and R4. Therefore, the reduction in the effective load-bearing area, load bypass around the hole, and localised deformation near the hole all have an accumulated and direct impact on the overall stiffness of the specimen.

The peak strain of the intact specimens was 1.04%, and forR3-R6, it increased to 1.22%, 1.23%, 1.24%, and 1.25% respectively. There is a relatively large difference between the intact and the holed specimens, and the increase in peak strain after R3 is significantly smaller. This shows that the introduction of a hole causes more pre-peak deformation and damage accumulation, and further enlargement of the hole has a reduced marginal effect on peak strain. In addition, there is a reduction in peak strength and elastic modulus; therefore, both the load-bearing capacity and deformation resistance will be lower. Although the pre-failure deformation has increased, due to the change in brittleness and the post-peak curve and loading stiffness, a complete evaluation should still be performed.

Table 2. Mechanical parameters of specimens with different hole diameters

Specimen	Holediameter /mm	Peakstrength /MPa	Elasticmodulus /GPa	Peakstrain /%	Strengthreduction /%
Intact	0	30.95	4.80	1.04	—
R3	6	18.73	2.95	1.22	39.48
R4	8	18.68	2.45	1.23	39.64
R5	10	17.34	2.10	1.24	43.97
R6	12	15.32	1.60	1.25	50.50

4. Macroscopic Failure Morphology of Sandstone with Different Hole Diameters



(a) I (b) R3 (c)R4 (d) R5 (d) R6

Figure 5. Macroscopic failure morphology of specimens with different hole diameters

Figure 5 shows the macroscopic failure morphologies of specimens with different hole diameters. The first sample had a shear fracture, and then a large inclined through-going crack and some other small cracks occurred. The failure surface is relatively flat, and the loss of stability in brittle fracture is sudden. A holey specimen has a hole-dominated failure mode, and generally, the cracks originate near the stress concentration point at the hole and then propagate to the upper and lower ends of the specimen. An Expansion of the Hole Diameter Alters the Position of Crack Initiation and Propagation. Near the hole, the wing cracks start to develop gradually, have irregular paths, and some specimens show crack deflection around the hole and the merging of multiple cracks.

The differences in failure morphology are consistent with the degradation of the mechanical properties mentioned above. Since there are no hole defects in the intact specimens, the load is carried by the intact matrix, and thus a high peak strength and elastic modulus are achieved before an abrupt shear-through failure. Due to the reduction in the effective load-bearing area and the concentration of stress at the hole in holed specimens, cracks are more likely to start at this location under a lower stress. Therefore, the elastic modulus is a decreasing function of the hole diameter. With an increase in the size of the hole, the path of a crack will be extended and more tortuous; consequently, a larger accumulation of deformation and damage is required before a through-hole failure surface is formed, and the peak strain will be elevated. In short, the failure mode has changed from the single-shear-controlled mode of the undamaged specimen to a mixed tension-shear mode near the hole. A Larger Hole Will Have a More Significant Effect on Crack Propagation and Disruption.

5. AE Activity and the Damage Process

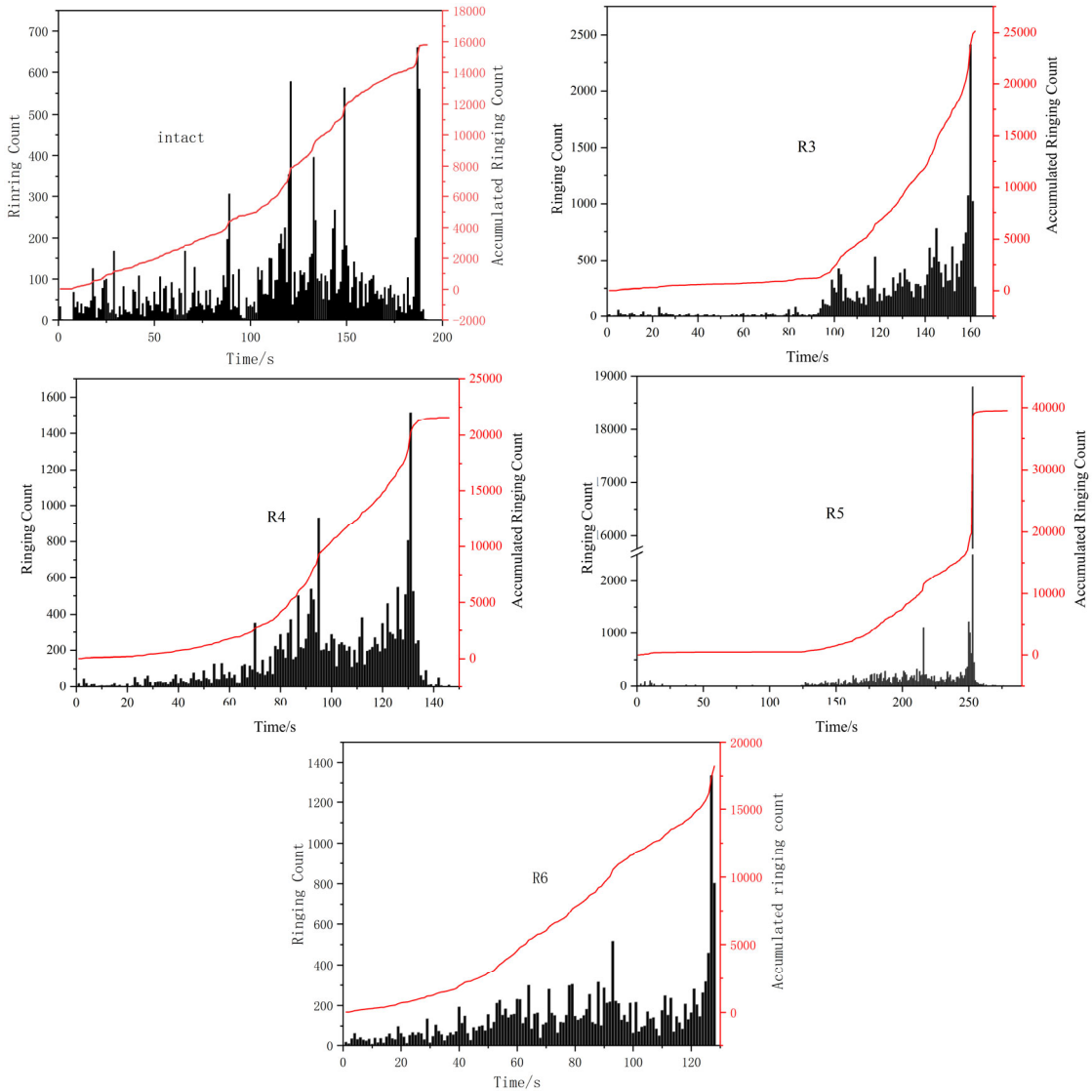


Figure 6. AE ring counts of specimens with different hole diameters

Figure 6 presents the evolution of AE ring counts and cumulative ring counts with time for specimens with different hole diameters. The intact specimens generate a certain number of low-amplitude ring signals during the initial loading stage. The ring count then fluctuates intermittently with time, while the cumulative curve rises slowly. As the failure nears, the number of rings suddenly increases to form a large peak, and at this time, the cumulative curve has begun to rise sharply and is no longer stable. The number of rings in the holed specimens is generally small and stable during the

early and middle stages of loading, and the cumulative curves are almost flat. Although there is a stress concentration at the hole, the start and spread of cracks are relatively late. Only when the peak stress is reached will there be a sudden increase in the ring count; otherwise, the two-stage pattern of quiescence followed by a sharp rise will occur.

An Increase in Hole Diameter Changes the Timing and Strength of AE Activity Significantly. R3, R4 and R6 all have a long period of low-ring-count quiescence before failure, and then a sudden increase and dense high peaks occur. R5 has a relatively long load time and a high cumulative ring count of about 4 x 10^4; furthermore, the number of rings is reached very late in the process. It is possible that the crack path is longer near the relatively large hole, and as a result, more damage has occurred. R6 is relatively small at its peak due to a large hole and a small number of cumulative ring counts. Therefore, the total number of AE events is not only related to the diameter of the hole but also affected by loading duration, crack propagation mode and the extent of specimen failure. AE activity in the holed specimens is concentrated closer to the failure point than in the undamaged specimens, and the AE signal intensity during the early non-linear stage is relatively low.

The evolution of AE is in line with the mechanical properties and large-scale failure features. The activity of AE in the intact specimens is distributed over time and relatively prolonged, reaches a high peak value and elastic modulus, and fails in a shear-through manner. In the holed specimens, the early AE quiescence shows that stress concentration at the hole has not yet led to significant crack propagation, but a sharp increase just before failure is associated with the rapid initiation, propagation and coalescence of wing cracks near the hole. With an increase in the diameter of the hole, both the difficulty of crack deflection around the hole and crack coalescence increase, and AE activity becomes more temporally concentrated. The damage caused by the hole is also different for the various cumulative ring numbers. AE ring-count characteristics may therefore serve as an auxiliary indicator for identifying damage stages and failure precursors in holed specimens, but they should be interpreted together with peak strength, elastic modulus, and failure morphology.

6. Energy Evolution

Under uniaxial compression, the energy evolution of a rock specimen follows the first law of thermodynamics. Assuming no heat exchange with the surroundings, all work performed by the external force is converted into internal strain energy. According to the energy-conservation principle, the total input strain-energy density U is composed of releasable elastic strain-energy density Ue and dissipated-energy density Ud. The calculation is given by the following equation:

$$U = U_e + U_d$$

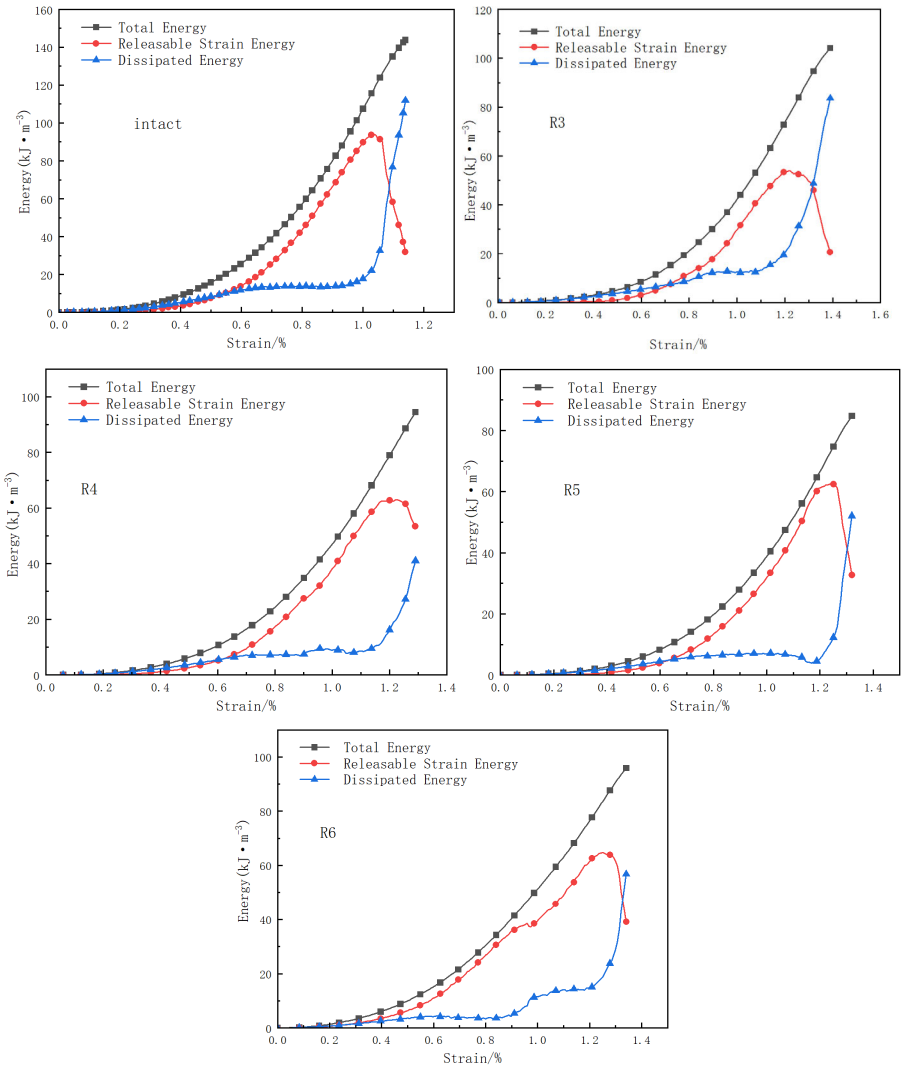


Figure 7. Energy-evolution curves of specimens with different hole diameters

The energy-evolution curves show that all specimens initially undergo slow accumulation of total strain energy, with dissipated energy remaining very low and increasing gradually. During this stage, most of the externally input energy is stored in the specimen as elastic strain energy. After the start of plastic deformation, the total strain energy increases at a higher rate and dissipated energy begins to rise significantly; thus, the formation and spreading of internal microcracks have started to dissipate energy. However, before reaching the maximum stress, a significant amount of releasable elastic strain energy is still present and provides the main energy for the final unstable failure. After reaching a peak, the load-bearing capacity declines sharply; thus, elastic strain energy is released rapidly and decreases significantly, while dissipated energy continues to rise due to the coalescence of macroscopic cracks and frictional sliding. The two parts are achieved at a relatively high speed, and then they drop due to brittle fracture.

The presence of a hole substantially changes the storage and dissipation of energy. Because of their relatively dense structure, the intact specimens can store higher total strain energy and elastic strain energy, and the proportion of elastic energy at the peak is the highest, corresponding to the most intense unstable failure. As the hole diameter increases, both total strain energy and peak elastic strain energy generally decrease, whereas the fraction of dissipated energy increases. This is mainly because stress concentration around the hole causes local regions to enter a plastic state earlier and induces microcrack initiation and propagation at a lower stress level, so that part of the input energy is dissipated through damage evolution before the peak. Among the different groups, large-hole specimens such as R6 show a more pronounced increase in dissipated energy before the peak and a lower efficiency of elastic-energy accumulation. This agrees with the decreases in peak strength and elastic modulus and the increase in peak strain described above, indicating that the hole defect not only reduces the energy-storage limit but also changes the pre-failure energy-dissipation mechanism, causing the specimen to undergo more complex damage evolution before failure.

7. Mechanistic Discussion of Infrared Precursors

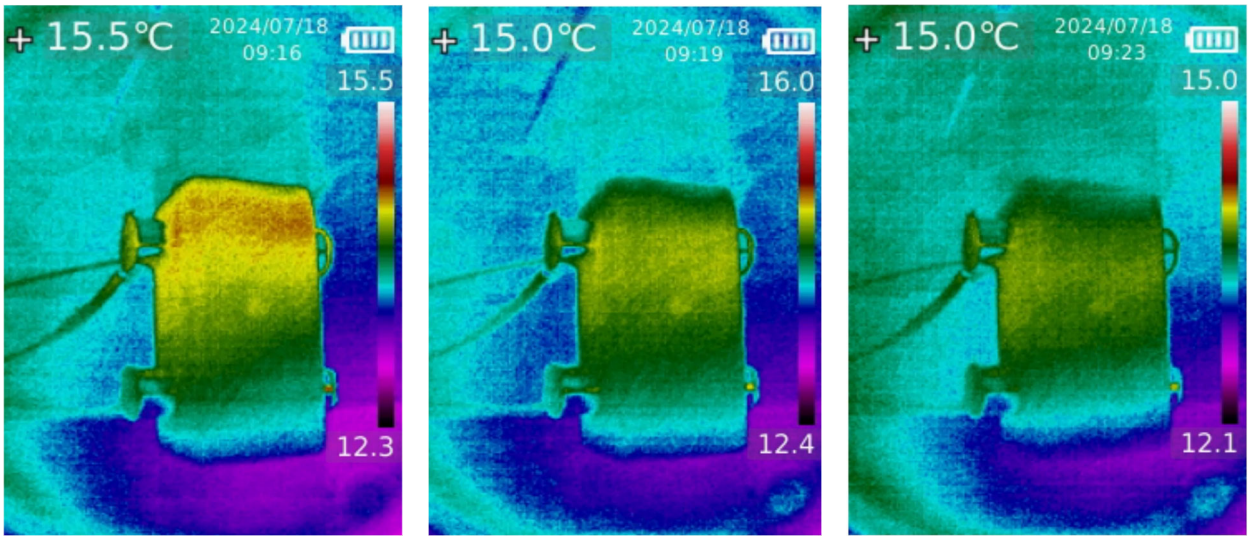


Figure 8. Infrared data for the R3 specimen at different times

Figure 8 presents infrared thermographs of the R3 specimen at different times; 09:23 corresponds to the state after the specimen had been crushed. The specimen surface shows a non-uniform radiation distribution in all three images. The upper and middle portions are predominantly yellow and yellow-green, whereas the lower portion gradually transitions to green and cyan. At 09:16, yellow and yellow-brown regions are more prominent in the upper part. At 09:19, the centre of the sample is a large yellow area, and a relatively cool green area has appeared in the upper part. As shown in Figure 8(09:23) after crushing the specimen, there is a relatively warm middle section and cooler upper and lower parts, but no obvious local high-temperature band has been identified. The ranges of the colour bars are 12.3-15.5 °C, 12.4-16.0 °C, and 12.1-15.0 °C, respectively, and the mapping from colour to temperature is different for each image. Therefore, the alteration of yellow areas cannot be used directly to infer actual warming or cooling. The readings in the upper-left corners are 15.5, 15.0, and 15.0 °C, respectively. Since the measurement position and the meaning of these readings are not specified, they cannot be considered the mean or maximum surface temperature of the specimen for comparison.

Overall, the thermograph of the crushed R3 specimen does not show a significant high-temperature anomaly that can be clearly identified by visual inspection. This observation does not imply that no temperature variation occurred during failure. Three static images are insufficient to capture a possible short-duration response at the instant of failure or to determine its temporal relationship with the peak load.

8. Discussion

8.1. Effects of Hole Diameter on Load Bearing and Deformation

In this test series, peak strength and elastic modulus of the holed sandstone generally decreased with increasing hole diameter, whereas peak strain was higher than that of the intact specimens. This indicates that loss of load-bearing capacity and increased cumulative pre-peak deformation occurred simultaneously, consistent with existing understanding of the effects of holes on rock mechanical

properties [4-5]. The mechanisms may involve changes in load-transfer paths and localized deformation induced by the hole, but the available data do not allow the stress distribution around the hole to be quantified. The differences in the strengths of the 6-mm and 8-mm groups are only 0.05 MPa, and without replicate tests, they should not be considered a strength plateau. An increase in peak strain alone does not show improved ductility; it must be combined with the post-peak response

8.2. Damage Activity and Infrared Response

All holed specimens exhibit enhanced AE activity in the latter stage of loading, along with a decrease in releasable elastic strain energy and an increase in dissipated energy in the energy curves. Fracture activity and energy redistribution in the failure process. However, AE counts do not increase steadily with the diameter of the hole, and the damage level of the large-hole specimens cannot be assumed to be higher based on this.

The thermograph of the R3 specimen after crushing does not show a distinct local high-temperature spot. Due to different colour-bar ranges in the three pictures, the alterations of colour cannot be identified as heat changes. Previous studies indicate that infrared responses in loaded sandstone are jointly controlled by multiple thermomechanical mechanisms and that anomaly identification requires background correction [9, 11]. The static thermographs in this test series are therefore insufficient to establish an infrared precursor or its temporal relationship with the increase in AE activity.

8.3. Engineering Implications and Limitations

The reduction in strength and stiffness accompanying an increase in hole diameter indicates that the load-bearing capacity of the remaining rock should be considered in pressure-relief-hole design. However, uniaxial compression of prefabricated holed specimens differs from actual borehole pressure relief under high in situ stress [3], and the strength reduction cannot be treated directly as a measure of pressure-relief efficiency. The present tests are insufficient to recommend an optimum hole diameter; the relevant trends require validation through replicate tests and synchronous local monitoring.

9. Conclusions

Using intact Qing sandstone and specimens containing stress-relief holes with diameters of 6, 8, 10, and 12 mm, and combining mechanical parameters, failure photographs, AE counts, energy curves, and infrared thermographs of the R3 specimen, the following conclusions were obtained.

(1) The peak strength of the tested specimens generally decreases with increasing hole diameter. The intact specimens had a peak strength of 30.95 MPa, whereas the four holed groups had values of 18.73, 18.68, 17.34, and 15.32 MPa, corresponding to reductions of 39.48%, 39.64%, 43.97%, and 50.50%, respectively. The strengths of the 6- and 8-mm groups are similar, but the present data do not establish a strength plateau or a critical hole diameter.

(2) Elastic modulus decreased from 4.80 GPa for the intact specimens to 1.60 GPa for the specimens with 12-mm holes, a reduction of 66.67%. The peak strains of the holed specimens were 1.22%-1.25%, higher than the 1.04% of the intact specimens. After a hole was introduced, load-bearing capacity and overall stiffness decreased while cumulative pre-peak deformation increased; these indicators alone are insufficient to determine a change in brittleness or ductility.

(3) Longitudinal, inclined, and branching cracks were observed in the holed specimens, and some crack bands were spatially associated with regions near the holes. AE activity intensified during the latter part of loading in all hole-diameter groups, but neither peak counts nor cumulative counts followed a consistent monotonic trend with hole diameter. The available photographs and count curves are insufficient to determine the sequence of crack initiation or the spatial distribution of damage.

(4) In the latter part of loading, the energy curves showed decreasing releasable elastic strain energy and increasing dissipated energy, indicating a redistribution of energy during failure. The available data are insufficient to confirm that the dissipated-energy fraction increases monotonically with hole diameter or to determine pressure-relief efficiency and the risk of dynamic instability for different hole diameters.

(5) The infrared thermograph of the R3 specimen after crushing did not show a prominent high-temperature band that could be clearly identified by visual inspection. Because the color-bar ranges differed among the three images and raw temperature measurements and synchronous records were unavailable, no clear infrared instability precursor was identified, and neither a hole-diameter-dependent warning sequence nor a threshold could be established.

References

[1] Ranjith, P. G., Zhao, J., Ju, M., De Silva, R. V., Rathnaweera, T. D., & Bandara, A. K. (2017). Opportunities and challenges in deep mining: A brief review. Engineering, 3(4), 546–551. https://doi.org/10.1016/j.eng.2017.04.024.

[2] Li, X., Gong, F., Tao, M., Dong, L., Du, K., Ma, C., Zhou, Z., & Yin, T. (2017). Failure mechanism and coupled static-dynamic loading theory in deep hard rock mining: A review. Journal of Rock Mechanics and Geotechnical Engineering, 9(4), 767–782. https://doi.org/10.1016/j.jrmge.2017.04.004

[3] Lu, X., Jiang, J., Wang, W., Cao, X., & Hong, L. (2023). Laboratory experimental study on the pressure relief effect of boreholes in sandstone under high-stress conditions. Sustainability, 15(21), 15557. https://doi.org/10.3390/su152115557

[4] Wu, H., Zhao, G., & Liang, W. (2019). Investigation of cracking behavior and mechanism of sandstone specimens with a hole under compression. International Journal of Mechanical Sciences, 163, 105084. https://doi.org/10.1016/j.ijmecsci.2019.105084

[5] Li, P., Ren, F. H., Cai, M. F., Guo, Q. F., Wang, H. F., & Liu, K. (2019). Investigating the mechanical and acoustic emission characteristics of brittle failure around a circular opening under uniaxial loading. International Journal of Minerals, Metallurgy, and Materials, 26(10), 1217–1230.

[6] Ma, L., Zhang, Y., Cao, K., & Wang, Z. (2019). An experimental study on infrared radiation characteristics of sandstone samples under uniaxial loading. Rock Mechanics and Rock Engineering, 52(9), 3493–3500. https://doi.org/10.1007/s00603-018-1688-6

[7] Wu, L., Liu, S., Wu, Y., & Wang, C. (2006). Precursors for rock fracturing and failure—Part I: IRR image abnormalities. International Journal of Rock Mechanics and Mining Sciences, 43(3), 473–482. https://doi.org/10.1016/j.ijrmms.2005.09.002

[8] Sun, H., Zhu, H. Y., Han, J., Fu, C., Chen, M. M., & Wang, K. (2023). Energy and infrared radiation characteristics of the sandstone damage evolution process. Materials, 16(12), 4342. https://doi.org/10.3390/ma16124342

[9] Sun, H., Zhu, H., Konietzky, H., Wang, F., & Herbst, M. (2022). Some thoughts about infrared radiation response characteristics during loading of sandstone samples. Applied Sciences, 12(23), 12229. https://doi.org/10.3390/app122312229

[10] Sun, H., Ma, L., Konietzky, H., Yuanyuan, D., & Wang, F. (2022). Characteristics and generation mechanisms of key infrared radiation signals during damage evolution in sandstone. Acta Geotechnica, 17(5), 1753–1763. https://doi.org/10.1007/s11440-021-01617-8

[11] Sun, H., Ma, L., Adeleke, N., & Zhang, Y. (2017). Background thermal noise correction methodology for average infrared radiation temperature of coal under uniaxial loading. Infrared Physics & Technology, 81, 157–165. https://doi.org/10.1016/j.infrared.2017.01.008

[12] He, M. C., Miao, J. L., & Feng, J. L. (2010). Rock burst process of limestone and its acoustic emission characteristics under true-triaxial unloading conditions. International Journal of Rock Mechanics and Mining Sciences, 47(2), 286–298. https://doi.org/10.1016/j.ijrmms.2009.09.003

[13] Liu, W., Ma, L., Sun, H., & Khan, N. M. (2021). An experimental study on infrared radiation and acoustic emission characteristics during crack evolution process of loading rock. Infrared Physics & Technology, 118, 103864. https://doi.org/10.1016/j.infrared.2021.103864

[14] Zhao, Y., & Jiang, Y. (2010). Acoustic emission and thermal infrared precursors associated with bump-prone coal failure. International Journal of Coal Geology, 83(1), 11–20. https://doi.org/10.1016/j.coal.2010.04.006

[15] Sun, X., Xu, H., He, M., & Zhang, F. (2017). Experimental investigation of the occurrence of rockburst in a rock specimen through infrared thermography and acoustic emission. International Journal of Rock Mechanics and Mining Sciences, 93, 250–259. https://doi.org/10.1016/j.ijrmms.2016.12.012